

Spray-drying Assisted Hydrothermal Synthesis of ZnIn₂S₄@GO as Anode Material for Improved Lithium ion Batteries

Zhi Zhang*, Zichuan Yi*, Liming Liu, Jianjun Yang, Chongfu Zhang, Xinjian Pan and Feng Chi

School of Electronic and Information Engineering, University of Electronic Science and Technology of China, Zhongshan Institute, Zhongshan 528402, China

*E-mail: zz001@zsc.edu.cn (Zhi Zhang), yizichuan@163.com (Zichuan Yi)

Received: 5 May 2020 / Accepted: 12 July 2020 / Published: 10 August 2020

In this work, flower-like ZnIn₂S₄ was synthesized via a hydrothermal reaction, and then a suspension of the ZnIn₂S₄ and commercial graphene oxide (GO) was spray-dried at 200 °C to obtain the ZnIn₂S₄@GO composite material. The ZnIn₂S₄ was completely wrapped by GO while its original spherical, flower-like structure was maintained. The GO coating could relieve the mechanical stress of volume changes during charge/discharge cycling of ZnIn₂S₄. Moreover, GO provided an additional channel for electron supply, thus improving conductivity and reversible capacity. The nanometric size and the binary metal sulfide nature of the ZnIn₂S₄ particles also contributed to improving the electrochemical behavior. The ZnIn₂S₄@GO anode showed excellent cycle performance with discharge capacity of 476.14 mAh g⁻¹ after 200 cycles at a current density of 500 mA g⁻¹. The excellent rate performance and cycling stability, both prove that the ZnIn₂S₄@GO composite is a highly suitable anode material for lithium ion batteries.

Keywords: Lithium ion batteries, Anode, ZnIn₂S₄@GO, spray-drying.

1. INTRODUCTION

Development and commercialization of lithium ion batteries (LIBs) has been a significant achievement to help cope with the increasing demand energy, especially for portable electronics. LIBs offer an environmentally friendly way to store energy with excellent energy density, wide operating temperature, and long life. However, graphite, a commercial anode material, has a theoretical specific capacity of 372 mAh g⁻¹, which is not high enough to be incorporated into the next-generation LIBs with high capacity cathodes [1-6]. Recently, metal sulfides, such as ZnS, Co₉S₈, FeS₂, and CuS, promise excellent theoretical energy densities and good electronic conductivities as anode materials [7-11]. Among these metal sulfides, zinc sulfide (ZnS), with the advantages of high theoretical specific capacity (962.3 mAh·g⁻¹), good stability, and environmental friendliness has been deeply investigated

for energy storage devices [12-15]. However, ZnS shows fast degradation of capacity due to volume expansion and contraction during cycling, thus, limiting its applicability.

Various strategies have been employed to address these challenges and researchers are trying to find effective ways to elevate its rate and cyclic performance. One of the most attractive approaches is to encapsulate sulfur into a carbon matrix, such as, with carbon nanotubes [12, 13], porous carbon [14, 15], and graphene [16, 17]. Among these carbon materials, graphene oxide (GO) is suitable for applications because it can restrain the volume expansion and improve the conductivity of the electrode [18-20]. In recent years, many studies have verified that the improvement in electronic conductivity of nanometric sized, binary metal sulfide anode materials significantly improve reversible capacity. For instance, Qu *et al.* reported that the initial capacity of mesoporous Cu_2SnS_3 microspheres is as high as $891 \text{ mAh}\cdot\text{g}^{-1}$ and shows a stable reversible capacity in subsequent cycles [21]. Yu *et al.* have successfully prepared NiCo_2S_4 nanotubes which can exhibit excellent discharge capacity ($720 \text{ mAh}\cdot\text{g}^{-1}$) after 50 cycles [22]. Kale *et al.* synthesized ZnIn_2S_4 /graphene using an *in situ* hydrothermal method. While ZnIn_2S_4 /graphene showed improved properties, there is still some loss of active material which results in poor cycling stability at high current density [23].

Based on literature and our previous studies on binary metal sulfides, we have synthesized flower-like ZnIn_2S_4 @GO microspheres via hydrothermal and spray-drying methods. The ZnIn_2S_4 can form reversible alloys with lithium and can yield a large theoretical capacity (713 mAh g^{-1}) based on conversion reactions [24]. The existence of GO in the composite can improve the Li^+ diffusion rate and prevent large volume changes on cycling. In context to high capacity cathode materials, the as-prepared ZnIn_2S_4 @GO composites are expected to become an advanced anode material for next-generation lithium ion batteries.

2. EXPERIMENTAL

2.1. Preparation of ZnIn_2S_4 and ZnIn_2S_4 @GO

The preparation methods of ZnIn_2S_4 and the ZnIn_2S_4 @GO composite are described in Figure 1. Typically, 0.13 g of zinc chloride (ZnCl_2), 0.6 g of hydrated indium nitrate ($\text{In}(\text{NO}_3)_3\cdot 4.5\text{H}_2\text{O}$) and 0.6 g of thioacetamide (TAA) were dissolved in 30 mL of distilled water and sonicated for 30 min. Then, the solution was transferred to a 50 mL autoclave and heated at $180 \text{ }^\circ\text{C}$ for 12 h. The resulting yellow powder was washed with distilled water and vacuum-dried at $50 \text{ }^\circ\text{C}$ for 6 h to obtain the ZnIn_2S_4 microspheres. The prepared ZnIn_2S_4 powder (1 g) was added to a solution of purchased GO (250 mL, 2 mg mL^{-1}) and sonicated for 30 min. This solution was then spray-dried at $200 \text{ }^\circ\text{C}$ to obtain a ZnIn_2S_4 @GO composite with flower-like morphology.

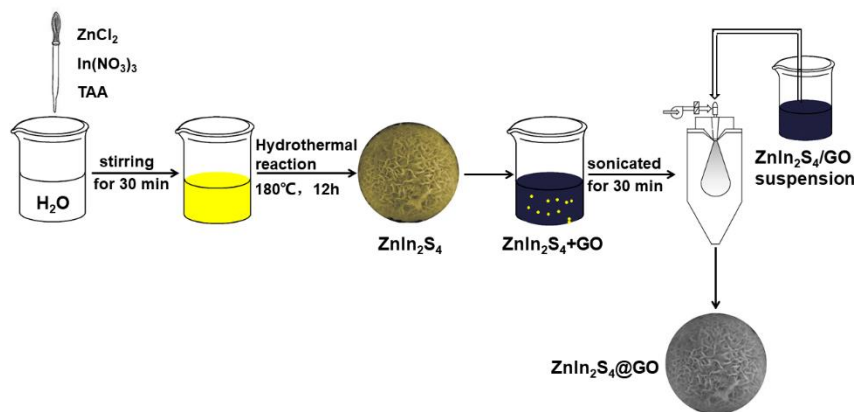


Figure 1. Schematic illustration of the synthesis of ZnIn₂S₄@GO.

2.2 Sample characterization

The as-prepared samples were studied by X-ray diffraction (XRD), with a D8 Discover, Bruker with Cu K α radiation. The structure and morphology of the composite were determined by a JEOL JSM-6700F scanning electron microscope (SEM) and a JEOL JEM-2100 transmission electron microscopy (TEM). The Raman spectra were obtained using a Lab RAM HR800 (Horiba). X-ray photoelectron spectroscopy (XPS) was implemented on the Thermo ESCALAB 250. Brunauer-Emmett-Teller (BET) measurements for the specific surface area and porosity of the samples were performed on a V-Sorb 2800P.

2.3 Electrochemical measurements

The prepared ZnIn₂S₄ and ZnIn₂S₄@GO powder (70 wt.%), polyvinylidene fluoride (20 wt.%) and super-P (10 wt.%) were mixed in 1-methyl-2-pyrrolidone and cast onto a copper foil with a scraper. The electrode film was dried in 60 °C for 12 h and cut into disks of 10 mm diameter. The electrochemical properties of ZnIn₂S₄ and ZnIn₂S₄@GO electrodes were characterized in a CR2032 battery configuration, assembled in an Ar-filled glovebox with lithium foil as the counter electrode. The electrolyte is 1 M LiPF₆ in a 1:1 v/v solution of ethylene carbonate (EC) and dimethyl carbonate (DMC), with Celgard 2400 as the separator. The charge and discharge cycle life of ZnIn₂S₄ and ZnIn₂S₄@GO electrodes was observed within a voltage range of 0.01~3.0 V vs Li/Li⁺ by using the BTS 4000. The electrochemical workstation (Princeton, Versa STAT4) was used to perform cyclic voltammetry (CV) at a scanning rate of 0.1 mV s⁻¹ between 0.01-3.0 V and electrochemical impedance spectroscopy (EIS) within a frequency range of 10 kHz to 10 mHz.

3. RESULTS AND DISCUSSION

The phase structure and the chemical states in the as-prepared ZnIn₂S₄ and the ZnIn₂S₄@GO composite were investigated by XRD, Raman, and XPS. The sharp diffraction peaks in Figure 2(a) indicate a high degree of crystallization, and all peaks correspond to the hexagonal phase of ZnIn₂S₄

(JCPDS No.65-2023). The XRD pattern of $\text{ZnIn}_2\text{S}_4@\text{GO}$ shows the corresponding characteristic peaks, which reveal that the process of spray-drying did not affect the crystal phase of ZnIn_2S_4 . Notably, the peak located at 11.5° could be attributed to the (002) plane of GO, indicating the successful introduction of GO to the composite.

Raman analysis was used to confirm the presence of the carbon material, as shown in Figure 2(b). The D band and G band in the Raman spectrum correspond to the two main peaks near 1343.92 cm^{-1} and 1590.25 cm^{-1} , respectively, thus, confirming incorporation of GO. The ratio of I_D/I_G for $\text{ZnIn}_2\text{S}_4@\text{GO}$ is found to be 0.98, which is slightly higher than that for GO, *i.e.*, 0.91. The ratio of I_D/I_G is an important parameter to estimate the degree of graphitization, and higher I_D/I_G values suggest a higher degree of graphitization and better conductivity of the as-prepared composite [25]. The $\text{ZnIn}_2\text{S}_4@\text{GO}$ composite was further characterized by XPS to determine the functional groups and elemental compositions, as shown in Figure 2(c)-(f). The high-resolution C $1s$ spectrum of the sample is demonstrated in Figure 2(c), three primary peaks at 284.8 eV, 286.9 eV, and 288.2 eV can be referred to as carbon atoms in C-C, C=O, and COOR, respectively.

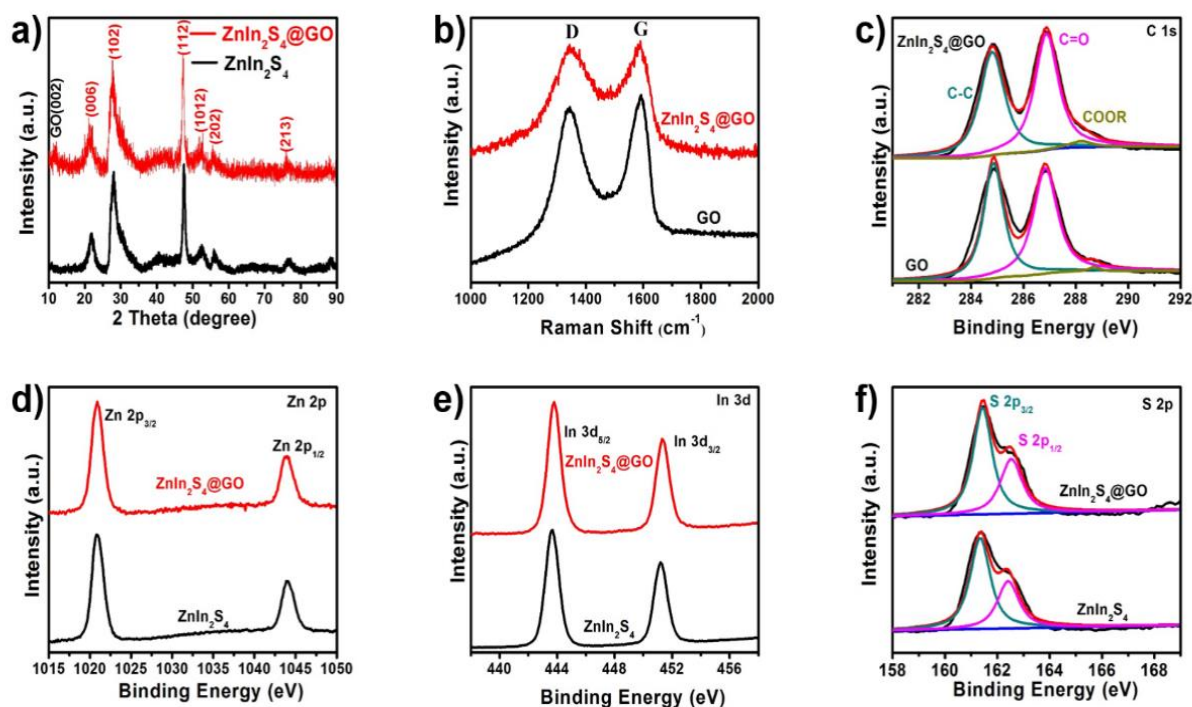


Figure 2. Characterization of the as-prepared ZnIn_2S_4 and $\text{ZnIn}_2\text{S}_4@\text{GO}$: a) Typical XRD pattern; b) Raman spectrum; c) XPS spectrum of C $1s$; d) XPS spectrum of Zn $2p$; e) XPS spectrum of In $3d$; and f) XPS spectrum of S $2p$.

The peak of an oxygen-containing functional group also demonstrates the existence of GO. As indicated in Figure 2(d), the peaks around 1021.0 eV and 1043.8 eV are classified as Zn $2p^{3/2}$ and Zn $2p^{1/2}$, which confirms the chemical state of Zn^{2+} . The binding energies around 443.7 eV and 451.3 eV in Figure 2(e) correspond to the observations in the XPS spectrum of In $3d$. Furthermore, the chemical

state of S atom was found to be in -2 state, *i.e.*, 161.6 eV and 162.5 eV correspond to S $2p^{3/2}$ and S $2p^{1/2}$ in Figure 2(f).

Nitrogen adsorption analyses show that the adsorption of N_2 by $ZnIn_2S_4@GO$ conformed to the type IV isotherm, as shown in Figure 3(a). The hysteresis loop shows that the pores in $ZnIn_2S_4@GO$ are slit-like and the BET surface area of $ZnIn_2S_4@GO$ was found to be $74.1 \text{ m}^2 \text{ g}^{-1}$. The rich, specific surface area offers enough active sites for the insertion and extraction of Li^+ . Figure 3(b) shows the pore size distribution of $ZnIn_2S_4@GO$, where a large number of pores at around 4 nm are present. The porous structure is beneficial for alleviating the mechanical stresses of volumetric expansion during charge-discharge cycling.

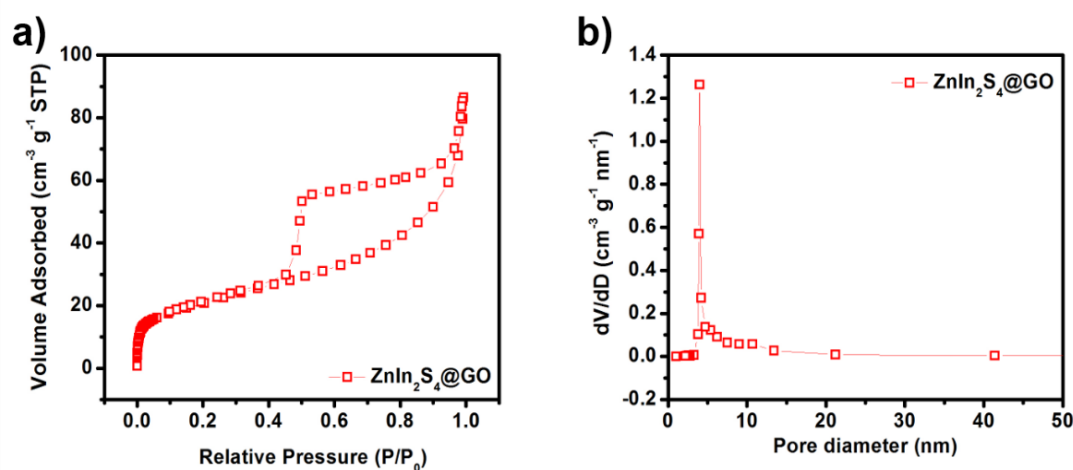


Figure 3. (a) The adsorption-desorption BET isotherms and (b) the pore size distribution of the $ZnIn_2S_4@GO$ composite.

The SEM images of $ZnIn_2S_4$ and $ZnIn_2S_4@GO$ are shown in Figure 4. The 3D flower-like structure is confirmed by Figure 4(a) and has a diameter of 3-6 μm , as shown in Figure 3(b). This 3D flower-like structure of $ZnIn_2S_4$ is formed by a large number of nanosheets, since clear gaps were observed between these sheets. The gaps can provide channels for the transport of the Li^+ and space for volume expansion during charge and discharge. The SEM images of the $ZnIn_2S_4@GO$ composite (Figure 4(c)-(d)), show that the $ZnIn_2S_4$ microspheres were completely wrapped by GO and while retaining the original structure.

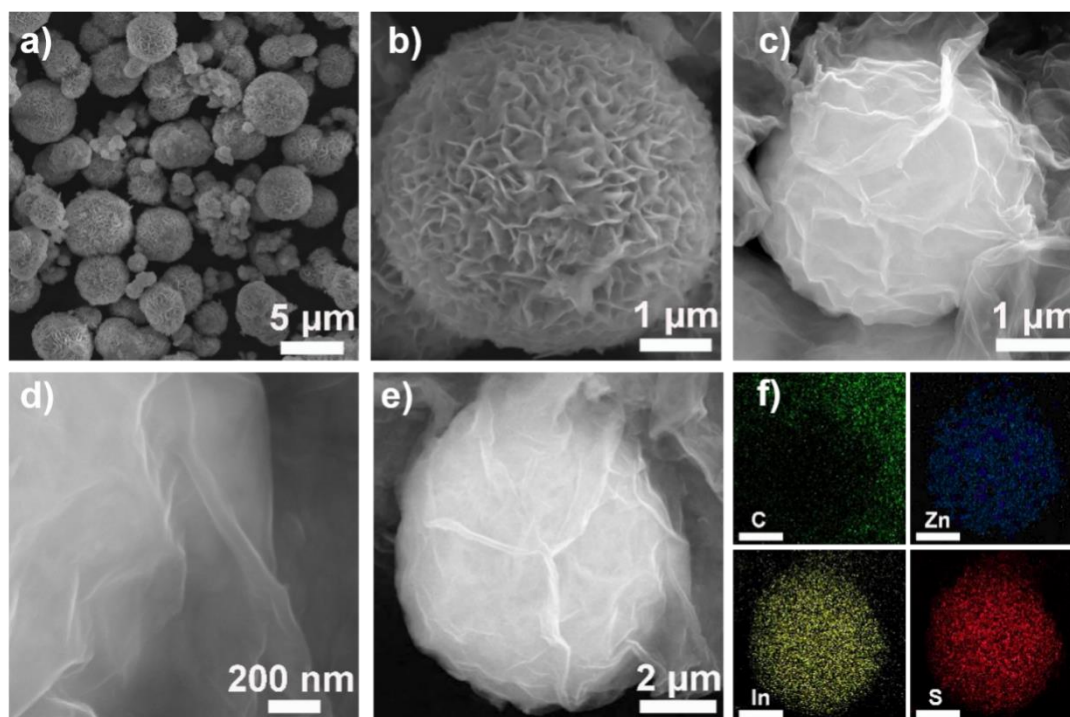


Figure 4. SEM images of ZnIn_2S_4 in (a)-(b) and $\text{ZnIn}_2\text{S}_4@\text{GO}$ in (c)-(e); and (f) the elemental mapping of image (e).

The successful encapsulation of GO is of great significance for the electrochemical performance of the $\text{ZnIn}_2\text{S}_4@\text{GO}$ electrode. The GO coating provides additional channels for the transport of Li^+ , thus, greatly relieving the volume expansion. Furthermore, the TEM images of $\text{ZnIn}_2\text{S}_4@\text{GO}$ composite in Figure 5 offer observations consistent with the SEM results. From the elemental mapping images of $\text{ZnIn}_2\text{S}_4@\text{GO}$ in Figure 4(e)-(f), it is clear that C, Zn, In, and S are distributed homogeneously, further confirming the successful synthesis of ZnIn_2S_4 and coating with GO.

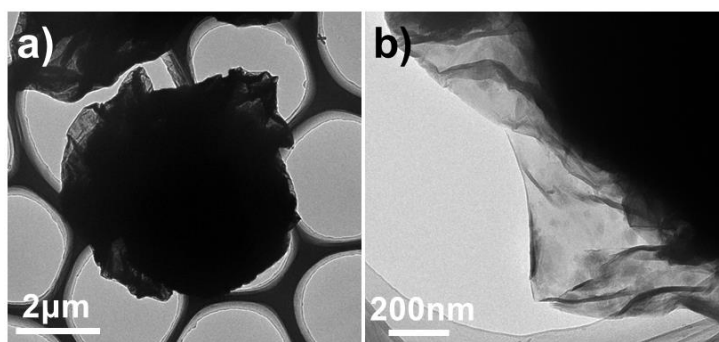


Figure 5. TEM images of as-prepared $\text{ZnIn}_2\text{S}_4@\text{GO}$ at different magnifications.

The enhanced electrochemical performance of ZnIn_2S_4 due to the GO coating is indicated clearly in the cycling performance comparison shown in Figure 6(a). The $\text{ZnIn}_2\text{S}_4@\text{GO}$ electrode

presented a higher capacity, of $476.14 \text{ mAh g}^{-1}$ after 200 cycles, while the ZnIn_2S_4 electrode provided only $173.02 \text{ mAh g}^{-1}$. The increase of specific capacity during discharge can mainly be attributed to the improved specific conductance and enhanced Li^+ diffusion rate caused by the flower-like ZnIn_2S_4 . In addition, during the electrochemical reaction process, the GO coating is said to have a non-negligible effect by providing additional Li^+ transport channels and restraining the volume expansion. The severe fluctuations for ZnIn_2S_4 , due to the cleavage and deactivation of active substances at high currents are absent. Additionally, the appearance of a solid electrolyte interface (SEI) film of the electrode surface reduces the initial capacity [26].

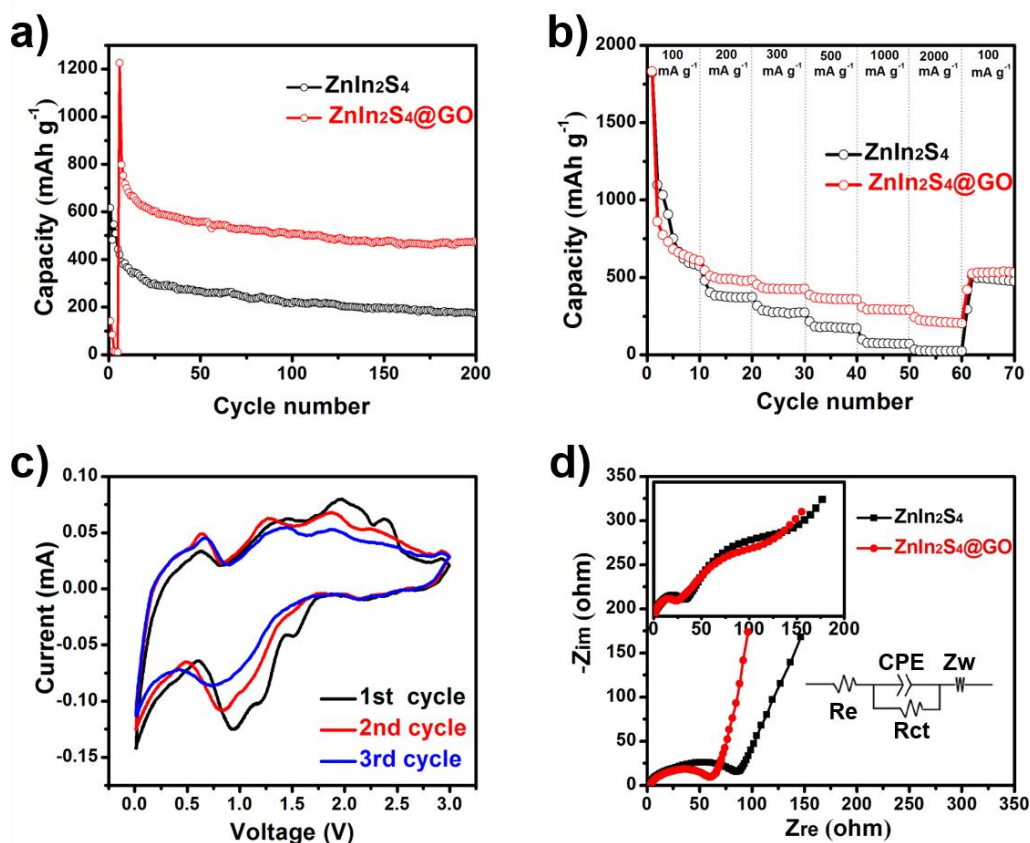


Figure 6. a) Charge/discharge cycle performance of ZnIn_2S_4 and $\text{ZnIn}_2\text{S}_4@\text{GO}$ composites at 500 mA g^{-1} ; b) Rate capability test of the ZnIn_2S_4 and $\text{ZnIn}_2\text{S}_4@\text{GO}$ cathodes at various current densities; c) CV curves of the $\text{ZnIn}_2\text{S}_4@\text{GO}$ cathode at 0.1 mV s^{-1} in a potential window of 0.01–3.0 V; d) Nyquist plots of ZnIn_2S_4 and $\text{ZnIn}_2\text{S}_4@\text{GO}$ electrodes in the range of 10 kHz–10 mHz at the 0th cycle and the 10th cycle.

Excellent reversible capacity and stable cycle performance of $\text{ZnIn}_2\text{S}_4@\text{GO}$ composites are also demonstrated by the rate capability in Figure 6(b). At different rates, *i.e.*, 100–2000 mA g^{-1} , the $\text{ZnIn}_2\text{S}_4@\text{GO}$ (and ZnIn_2S_4) anode show capacities 608.4 (572.5), 481.3 (373.5), 424.7 (274.1), 357.0 (170.0), 288.5 (70.4), and 241.3 (21.2) mAh g^{-1} , respectively. The capacity of the ZnIn_2S_4 anode is seen to decline significantly more rapidly than the $\text{ZnIn}_2\text{S}_4@\text{GO}$. Compared to ZnIn_2S_4 , the $\text{ZnIn}_2\text{S}_4@\text{GO}$ composite shows more efficient electron conductivity due to GO during the charge/discharge process. Moreover, a capacity of 529.9 (473.1) mAh g^{-1} was attained when the

current density returned to 100 mA g^{-1} . Both ZnIn_2S_4 and $\text{ZnIn}_2\text{S}_4@\text{GO}$ electrodes show excellent rate performance, which can be associated with the 3D hierarchical structure of ZnIn_2S_4 .

The lithium storage mechanism of the $\text{ZnIn}_2\text{S}_4@\text{GO}$ electrode was further analyzed by cyclic voltammetry (CV) measurements at 0.1 mV s^{-1} in a potential window of 0.01-3.0 V. Figure 6(c) shows the CV curves for the first, second, and third cycles of $\text{ZnIn}_2\text{S}_4@\text{GO}$ electrode. A huge capacity consumption occurred at the 1st cycle, which is consistent with the cycling and rate performance measurements. From the second cycle onwards, the electrodes showed stable capacities, indicating excellent reversible performance. In the first cathodic scan, the peaks at 1.6 and 0.95 V refer to the reduction of ZnIn_2S_4 to In, Zn and formation of Li_2S . Another broad cathodic peak between 0.6 and 0.05 V is ascribed to subsequent reaction of Li^+ with Zn and In metal. During anodic scanning process, the peak at 0.5 V is due to delithiation from Zn alloy, whereas peak at higher 1.2 V is due to delithiation from Li_xIn . The additional oxidation peaks in 1.5-2.5 V are caused by multi-step regeneration of zinc sulfide and indium sulfide [23].

In the Nyquist diagram (Figure 6d), the semicircles at high and at intermediate frequency correspond to the electrolyte resistance (R_e) and the charge transfer resistance (R_{ct}), respectively [27]. The sloped line in the low-frequency area is called the Warburg resistance (Z_w). As shown in Figure 6d, both curves display similar semicircles; ZnIn_2S_4 (87.1Ω) showed a higher charge transfer resistance than $\text{ZnIn}_2\text{S}_4@\text{GO}$ (60.8Ω), suggesting that the incorporation of GO was beneficial for a faster interfacial charge transfer and higher reaction kinetics [28]. The $\text{ZnIn}_2\text{S}_4@\text{GO}$ composite with higher reversible capacitance, high cycling stability, and excellent rate performance is expected to become a suitable candidate for high-performance LIBs.

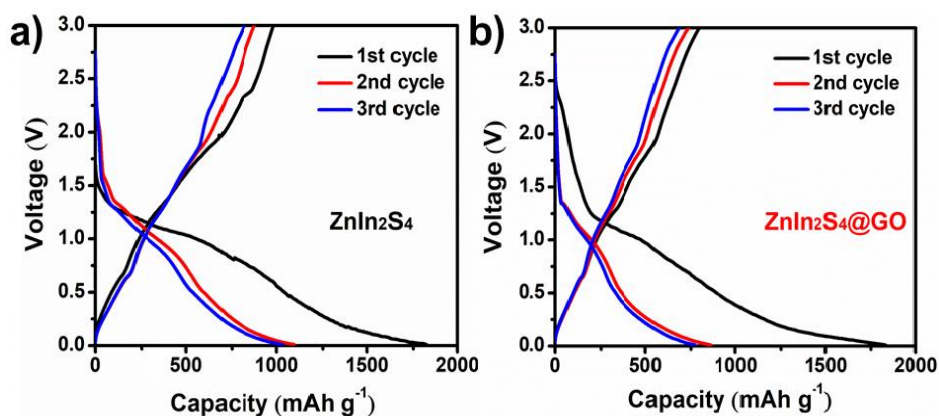


Figure 7. Discharge/charge voltage profiles of (a) ZnIn_2S_4 and (b) $\text{ZnIn}_2\text{S}_4@\text{GO}$ at 100 mA g^{-1} .

The representative charge/discharge profiles of ZnIn_2S_4 and $\text{ZnIn}_2\text{S}_4@\text{GO}$ electrodes at 100 mA g^{-1} are shown in Figure 7. The charge/discharge voltage plateaus agree well with the CV results. From the second cycle onwards, both ZnIn_2S_4 and $\text{ZnIn}_2\text{S}_4@\text{GO}$ present a much more stable electrochemical behavior, with the $\text{ZnIn}_2\text{S}_4@\text{GO}$ electrodes performing significantly better. The $\text{ZnIn}_2\text{S}_4@\text{GO}$ electrode shows a high initial capacity of 1830 mAh g^{-1} at first cycle. The specific capacity is superior to most of the literature reports of metal sulfide-based anodes, such as NiS-PPy-

CNF film (635 mAh g^{-1}) [29], cobalt sulfide/carbon nanotubes (814 mAh g^{-1}) [30], ZnS/graphene composites (1464 mAh g^{-1}) [31], and core-shell-like ZnS/C nanocomposite (1277 mAh g^{-1}) [32].

To study the structural stability of ZnIn_2S_4 and $\text{ZnIn}_2\text{S}_4@\text{GO}$ electrodes, their surface morphologies, after 100 cycles, were observed by SEM (Figure 8). The structure of ZnIn_2S_4 appeared broken and agglomerated after cycling. On the other hand, the $\text{ZnIn}_2\text{S}_4@\text{GO}$ electrode maintained good structural integrity without any visible agglomeration, suggesting that the $\text{ZnIn}_2\text{S}_4@\text{GO}$ adapted well to the volume changes on cycling, which is beneficial to improve the cycling performance. The structural stability can be attributed to the introduction of GO, which prevents the separation and agglomeration of ZnIn_2S_4 nanosheets during the cycle, which ultimately contributes to the long cycle stability [33].

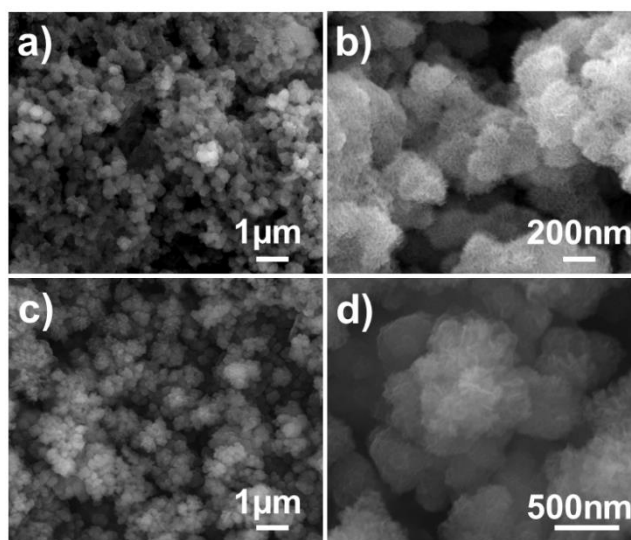


Figure 8. The SEM images of ZnIn_2S_4 in (a)-(b), and $\text{ZnIn}_2\text{S}_4@\text{GO}$ in (c)-(d), after 100 cycles.

Table 1. Comparison of various electrochemical properties of previously reported materials with our work.

Electrode material	Current density (discharge)	Reversible capacity (mAh g^{-1})	Cycle No.	Reference
ZnO nanosheets	500 mA g^{-1}	400	100	[34]
ZnO-CoO-C	0.5 C	438	50	[35]
ZnO@ZnS	200 mA g^{-1}	513.4	100	[36]
GZIS2	150 mA g^{-1}	454	100	[23]
ZnS/C	100 mA g^{-1}	570	150	[37]
ZnS@graphite	100 mA g^{-1}	444	300	[38]
$\text{Co}_3\text{S}_4\text{-ZnS/NC}$	100 mA g^{-1}	409.5	200	[39]
In_2S_3 nanosheets	700 mA g^{-1}	450	40	[40]
$\text{In}_2\text{S}_3@\text{N-Carbon}$	100 mA g^{-1}	485	200	[41]
$\text{ZnIn}_2\text{S}_4@\text{GO}$	500 mA g^{-1}	476.14	200	This work

The charge density, reversible capacity, and number of cycles of the ZnIn₂S₄@GO anode were compared with other materials reported in literature, in Table 1. The results indicate that the ZnIn₂S₄@GO anode exhibits a good cycling performance, provides a high and stable specific capacity of discharge (500 mA g⁻¹) and low capacity fading even at the 200th cycle. The improvement in performance of the ZnIn₂S₄@GO anode was due to the synergistic effect of ZnIn₂S₄ and GO coating. The GO conductive network can effectively manage the volume changes and furnish additional electron transfer channels for electrons and Li⁺ [28]. Meanwhile, flower-like ZnIn₂S₄ also acted as buffer to alleviate volume changes while cycling and improved reversible capacity and hence to maintain the long cycle-life performance of the batteries.

4. CONCLUSIONS

The flower-like ZnIn₂S₄ material was synthesized by a hydrothermal way, followed by spray-drying to prepare a ZnIn₂S₄@GO composite. The ZnIn₂S₄ was completely wrapped by GO and retained the original flower-like structure. The as-synthesized ZnIn₂S₄@GO composites displayed a high reversible capacity and steady cycle performance. The GO coating is expected to contribute to the improvement in conductivity of the ZnIn₂S₄@GO composite, and thus, greatly reduce the extent of volume expansion. The 3D flower-like ZnIn₂S₄, with nanometric size, can promote the migration of Li⁺ and provide a rich specific surface area. The synergy between ZnS, In₂S₃, and GO results in excellent electrochemical performance of the ZnIn₂S₄@GO composite. In addition, the synthesis method presented in this paper is simple, efficient, and highly suitable for large-scale production.

ACKNOWLEDGEMENTS

This research was funded by the Youth Innovative Talent Project of Guangdong Education Department (No.2017KQNCX243, No.2017KQNCX245), Science and Technology Project Foundation of Zhongshan (No.2017B1128, No.2018B1117), the High Level Talent Research Starting Project in University of Electronic Science and Technology of China Zhongshan Institute (No. 417YKQ07, No.417YKQ03), the Guangdong Basic and Applied Basic Research Foundation (No. 2020A1515010420), the Key Research Platforms and Research Projects in Universities and Colleges of Guangdong Provincial Department of Education (No. 2018KQNCX334), Zhongshan Innovative Research Team Program (No. 180809162197886), Project for Innovation Team of Guangdong University (No. 2018KCXTD033), National Key R&D Program of China (No. 2018YFB0407100-02), National Natural Science Foundation of Guangdong Province (No. 2018A030310662).

References

1. K. N. Dinh, Q. Liang, C.F. Du, J. Zhao, A. I. Y. Tok, H. Mao and Q. Yan, *Nano Today*, 25 (2019) 99.
2. B. Li, Y. Wang, H. Lin, J. Liu, L. Xing, M. Xu and W. Li, *Electrochim. Acta*, 141 (2014) 263.
3. Q. Wang, L. Jiang, Y. Yu and J. Sun, *Nano Energy*, 55 (2019) 93.
4. J. Zhang, G. Li, Y. Zhang, W. Zhang, X. Wang, Y. Zhao, J. Li and Z. Chen, *Nano Energy*, 64 (2019) 103905.
5. C. Zhai, N. Du, H. Zhang, J. Yu and D. Yang, *ACS Appl. Mater. Interfaces*, 3 (2011) 4067.

6. Y. Tian, Y. Zhao, Y. Zhang, L. Ricardez-Sandoval, X. Wang and J. Li, *ACS Appl. Mater. Interfaces*, 11 (2019) 23271.
7. Y. Zhou, D. Yan, H. Xu, J. Feng, X. Jiang, J. Yue, J. Yang and Y. Qian, *Nano Energy*, 12 (2015) 528.
8. R. Jin, J. Zhou, Y. Guan, H. Liu and G. Chen, *J. Mater. Chem. A*, 2 (2014) 13241.
9. L. Xu, Y. Hu, H. Zhang, H. Jiang and C. Li, *ACS Sustainable Chem. Eng.*, 4 (2016) 4251.
10. L. Li, M. Cabán-Acevedo, S. N. Girard and S. Jin, *Nanoscale*, 6 (2014) 2112.
11. K. Jiang, Z. Chen and X. Meng, *ChemElectroChem*, 6 (2019) 2825.
12. X. Du, H. Zhao, Z. Zhang, Y. Lu, C. Gao, Z. Li, Y. Teng, L. Zhao and K. Świerczek, *Electrochim. Acta*, 225 (2017) 129.
13. Z. Chen, R. Wu, H. Wang, Y. Jiang, L. Jin, Y. Guo, Y. Song, F. Fang and D. Sun, *Chemical Engineering Journal*, 326 (2017) 680.
14. H. Chen, B. Zhang, Y. Cao, X. Wang, Y. Yao, W. Yu, J. Zheng, J. Zhang and H. Tong, *Ceram. Int.*, 44 (2018) 13706.
15. Y. Fu, Z. Zhang, X. Yang, Y. Gan and W. Chen, *RSC Adv.*, 5 (2015) 86941.
16. M. Mao, L. Jiang, L. Wu, M. Zhang and T. Wang, *J. Mater. Chem. A*, 3 (2015) 13384.
17. R. Zhang, Y. Wang, M. Jia, J. Xu and E. Pan, *Appl. Surf. Sci.*, 437 (2018) 375.
18. H. Peng, X. Wang, Y. Zhao, T. Tan, Z. Bakenov and Y. Zhang, *Polymers*, 10 (2018) 399.
19. Y. Tian, Z. Sun, Y. Zhang, X. Wang, Z. Bakenov and F. Yin, *Nanomaterials*, 8 (2018) 50.
20. Y. Zhang, Y. Zhao and Z. Bakenov, *Ionics*, 20 (2014) 1047.
21. B. Qu, M. Zhang, D. Lei, Y. Zeng, Y. Chen, L. Chen, Q. Li, Y. Wang and T. Wang, *Nanoscale*, 3 (2011) 3646.
22. D. Yu, Y. Yuan, D. Zhang, S. Yin, J. Lin, Z. Rong, J. Yang, Y. Chen and S. Guo, *Electrochim. Acta*, 198 (2016) 280.
23. S. B. Kale, R. S. Kalubarme, M. A. Mahadadalkar, H. S. Jadhav, A. P. Bhirud, J. D. Ambekar, C.J. Park and B. B. Kale, *PCCP*, 17 (2015) 31850.
24. L. Ye, J. Fu, Z. Xu, R. Yuan and Z. Li, *ACS Appl. Mater. Interfaces*, 6 (2014) 3483.
25. R. Wang, S. Gao, K. Wang, M. Zhou, S. Cheng and K. Jiang, *Sci. Rep.*, 7 (2017) 7963.
26. R. Liu, C. Shen, C. Zhang, J. Iocozzia and Q. Wang, *J. Mater. Sci.*, 53 (2018) 8499.
27. J. Huang and W. Liu, *J. Taiwan Inst. Chem. Eng.*, 96 (2019) 205.
28. H. Li, B. Zhang, Q. Zhou, J. Zhang, W. Yu, Z. Ding, M. Tsiamtsouri, J. Zheng and H. Tong, *Ceram. Int.*, 45 (2019) 7830.
29. X. Li, Y. Chen, J. Zou, X. Zeng, L. Zhou, and H. Huang, *J. Power Sources*, 331 (2016) 360.
30. H. Wang, J. Ma, S. Liu, L. Nie, Y. Chai, X. Yang and R. Yuan, *J. Alloys Compd.*, 676 (2016) 551.
31. M. Mao, L. Jiang, L. Wu, M. Zhang and T. Wang, *J. Mater. Chem. A*, 3 (2015) 13384.
32. X. Du, H. Zhao, Y. Lu, Z. Zhang, A. Kulka and K. Świerczek, *Electrochim. Acta*, 228 (2017) 100.
33. J. Yao, B. Liu, S. Ozden, J. Wu, S. Yang, M. F. Rodrigues, K. Kalaga, P. Dong, P. Xiao, Y. Zhang, R. Vajtai and P. M. Ajayan, *Electrochim. Acta*, 176 (2015) 103.
34. X. Huang, X. Xia, Y. Yuan and F. Zhou, *Electrochim. Acta*, 56 (2011) 4960.
35. Z. Wu, L. Qin and Q. Pan, *J. Alloys Compd.*, 509 (2011) 9207.
36. H. Li, J. Wang, Y. Zhao and T. Tan, *Energies*, 11 (2018) 2117.
37. A. Park, K. Jeon and C. Park, *Electrochim. Acta*, 265 (2018) 107.
38. J. Yoon, I. T. Kim, J. Bae and J. Hur, *J. Ind. Eng. Chem.*, 76 (2019) 258.
39. Z. Zhang, Y. Huang, X. Liu, C. Chen, Z. Xu and P. Liu, *Carbon*, 157 (2020) 244.
40. F. Ye, C. Wang, G. Du, X. Chen, Y. Zhong and J. Z. Jiang, *J. Mater. Chem.*, 48 (2012) 24959.
41. L. Sun, X. Liu, T. Ma, L. Zheng, Y. Xu, X. Guo and J. Zhang, *Solid State Ionics*, 329 (2019) 8.